Transactions of Materials Research 1 (2025) 100005

Contents lists available at ScienceDirect

Transactions of Materials Research

journal homepage: www.sciencedirect.com/journal/transactions-of-materials-research

Three-dimensional ultrasounds bring about crystallographic microstructure transition and mechanical performance synergy for multicomponent $(FeCoNiCr)_{85}Mo_{15}$ eutectic alloy

W.J. Gao, X. Wang, J.Y. Wang, W. Zhai *, B. Wei

MOE Key Laboratory of Materials Physics and Chemistry Under Extraordinary Conditions, School of Physical Science and Technology, Northwestern Polytechnical University, Xi'an, 710072, China

ARTICLE INFO

Keywords:
Eutectic structure
Multicomponent alloy
Ultrasonic solidification
Crystallographic relation
Mechanical property

ABSTRACT

Three-dimensional (3D) ultrasounds were applied to the solidification process of multicomponent $(FeCoNiCr)_{85}Mo_{15}$ eutectic alloy. At the small ultrasonic amplitude of 14 μm, the lamellar (γ+σ) eutectic was significantly refined, and the interface orientation was shifted from $[001]_\gamma//[112]_\sigma$ and $(-110)_\gamma//(11\text{-}1)_\sigma$ to the most stable configuration of $[011]_\gamma//[\text{-}110]_\sigma$ and $(\text{-}11\text{-}1)_\gamma//(001)_\sigma$. If ultrasonic amplitude was increased, σ phase transferred from tetragonal to hexagonal close-packed (HCP) structure, while its independent nucleation and growth facilitated the formation of anomalous (γ+σ) eutectics. Once the ultrasonic amplitude reached 16 μm, a metastable μ phase enriched with Cr element was found in the form of lamellar (γ+μ) eutectic structure. These crystallographic structure transitions were attributed to the ultrasound induced high energy and nonlinear cavitation and acoustic streaming effects. The diverse eutectic structures obtained by 3D ultrasonic solidification brought in superior mechanical properties. The maximum yield strength and ductility were enhanced by 1.4 and 2.1 times to 2000 MPa and 21.4 %, respectively. The strengthening mechanism belonged to the refinement of lamellar (γ+σ) eutectics and the stable interface configuration secured by weak ultrasounds, whereas the increased volume fraction of the FCC-structured γ phase in (γ+σ) eutectic and the metastable (γ+μ) eutectic structure formed under strong ultrasounds contributed to enhance alloy ductility.

1. Introduction

Since eutectic structures facilitate the optimal balance between high strength and exceptional ductility, multicomponent eutectic alloys have attracted significant attention in recent years for their promising mechanical properties and potential applications [1–4]. With the development of alloy design and diverse demands for multicomponent alloys, researchers have explored the addition of refractory elements such as Mo, Nb, Ta and W into FeCoNiCr-based alloys to further enhance the alloy's strength, thermal stability and wear resistance [5–11]. For example, $FeCoNiCrNb_{0.5}$, $FeCoNiCrTa_{0.4}$ and $(FeCoNiCr)_{85}Mo_{15}$ alloys containing FCC and intermetallic phases with high hardness exhibit exceptional work-hardening behavior and excellent high-temperature stability, thereby broadening the mechanical performance spectrum of multicomponent eutectic alloys and enhancing their potential for advanced applications.

In addition to compositional modifications, the optimization of multicomponent eutectic alloys performance also comes from microstructure regulation. The distinctive characteristics including the phase constitution, the volume fraction and the crystal structure of each eutectic phase, and the orientation relationships at eutectic interfaces jointly determine mechanical performance [12–15]. For example, Wang et al. [13] obtained good mechanical properties in $Al_{17}Ni_{34}Ti_{17}V_{32}$ alloy at both room and elevated temperatures through eutectic structure modulation with ultrafine lamellar and low-mismatch eutectic interfaces. Based on theoretical calculations, Zhou et al. [15] demonstrated that balancing the phase fractions of FCC and BCC eutectic phases could enhance the tensile strength and work-hardening capability for the $FeCoNi_{2.1}CrAl$ alloy.

Applying ultrasound during alloy solidification to modulate microstructure and improve performances has a well-documented history [16–21]. Numerous studies have established that ultrasonic solidification provides considerable advantages, such as grain structure refinement [22,23], segregation mitigation [24,25], and mechanical property

* Corresponding author.
E-mail address: zhaiwei322@nwpu.edu.cn (W. Zhai).

https://doi.org/10.1016/j.tramat.2025.100005
Received 21 March 2025; Received in revised form 1 April 2025; Accepted 1 April 2025
Available online 3 April 2025

enhancement [26,27]. However, the majority of existing research primarily concentrates on conventional alloys, with limited investigations into high-temperature multicomponent alloys. Currently, we have conducted studies on the ultrasonic solidification of $FeCoNi_{2.1}CrAl$ and $FeCoNi_2Al_{0.9}$ alloys [24,28]. The research indicates that high-power ultrasound can refine eutectic and enhance the coherent degree of the Kurdjumov-Sachs (K-S) orientation between the FCC and BCC eutectic phases, which simultaneously result in the overall improved performance. However, in contrast to the BCC phase, intermetallic compounds typically possess more complex and highly ordered crystal structures, along with higher melting points and superior high-temperature stability [29]. Therefore, it speculates that the intensive nonlinear effects of ultrasound may induce unexpected changes in the interface orientation or phase structures in multicomponent eutectic alloys comprising FCC and intermetallic phases.

In this work, by utilizing a self-designed ultrasonic solidification system for high-temperature alloys, three-dimensional (3D) ultrasounds with 20 kHz frequency were applied throughout the solidification process of $(FeCoNiCr)_{85}Mo_{15}$ alloy. The eutectic microstructure and crystallographic characteristics were carefully analyzed to reveal out the dynamic solidification mechanism of the (FCC + intermetallic)-type eutectic within ultrasound field. The relationship between the ultrasound-tuned eutectic microstructure and mechanical property was also clarified.

2. Experimental procedure and numerical simulation

2.1. Three-dimensional ultrasonic solidification and microstructure characterization

The $(FeCoNiCr)_{85}Mo_{15}$ alloy samples were prepared by arc melting for five times with purity of 99.99 % Fe, 99.99 % Co, 99.99 % Ni, 99.99 % Cr and 99.99 % Mo elements in proportion to the composition. The experiments were performed by self-designed 3D ultrasonic solidification apparatus for metallic alloys [18]. Before the experiment, the ultrasonic transducers with a 20 kHz driving frequency were arranged in the X, Y and Z directions by locating TC4 ultrasonic horns perpendicularly at the center of the graphite mold walls through elastic contact. The size of the mold and ultrasonic horns were well-designed to keep the whole system in the resonance state. During the experimental process, the master alloy sample was inductively heated to 1773 K, which was then poured into a rectangular graphite mold with an internal size of 20 × 20 × 50 mm preheated to 1173 K. The three orthogonal ultrasound transducers were simultaneously switched on to introduce ultrasound waves with the same amplitudes of 14, 16, and 18 μm into the solidification process until the alloy temperature monitored by a type K NiCr-NiSi thermocouple reached 1273 K. Afterwards, the power ultrasound sources were turn off and the solidified alloy samples were naturally cooled down to room temperature.

The acoustic signal in the solidifying alloy was measured synchronously by a self-designed high-temperature sound field detecting system [18,30]. The validity of this detecting system was confirmed by a standard commercial TC4035 hydrophone. A quartz waveguide rod in 4 mm diameter was inserted at 3 mm away from the side wall of the solidifying alloy sample with the submergence depth of 30 mm to collect local acoustic signals. These signals were captured by the acquisition card and processed by a self-compiled analysis program. The acoustic spectra of frequency domain with the bandwidth of 0~1 MHz and a resolution of 0.03 kHz were obtained, and the stable/transient cavitation intensities were further calculated by integrating different frequency bands.

After experiment, the solidified alloy samples were cut longitudinally and polished. A Netzch 404C Differential Scanning Calorimeter (DSC) was used for thermal analysis of statically and ultrasonically solidified alloy specimens at a scan rate of 10 K/min. The phase constitution was analyzed by a D8 discover A25 X-ray diffractometer (XRD) with Co target. The microstructural morphology, compositional identification, and crystallographic analyses were carried out on a Tescan Clara GMH scanning electron microscope (SEM) equipped with an Oxford Nordly spectrometer and an electron back scattered diffraction (EBSD) detector. The residual stress of EBSD specimens were eliminated by mechanical vibration on VibroMet 2 equipment for 8h. Mechanical tests were performed at the compression rate of 1×10^{-3} s^{-1} by an Instron 3382 universal testing machine with the sample size of Φ 4 × 6 mm. A FEI Talos F200X transmission electron microscope (TEM) was used to characterize morphology and crystallographic structure. The TEM specimen was prepared by a Fischione Model 110 automatic Twin-Jet Electropolisher at room temperature after uniformly polishing to 50 μm. All solidification experiments and mechanical tests were repeated more than three times to ensure the repeatability of results.

2.2. Numerical simulation of acoustic and flow fields

The Comsol Multiphysics software was employed to develop a geometric model for the analysis of acoustic streaming field distribution in liquid $(FeCoNiCr)_{85}Mo_{15}$ alloy. The vibration of the graphite casting mold induced by 3D ultrasound with 14, 16, and 18 μm amplitudes were calculated by the solid mechanics module. The result was provided as the excitation to calculate the sound distribution by pressure acoustic module using a nonlinear inhomogeneous Helmholtz equation considering the energy loss caused by the cavitation effect [31]:

$$\nabla^2 P + k_c^2 P = 0, \tag{1}$$

where P and k_c represent the sound pressure and the acoustic wave vector, respectively. The square of k_c satisfies the following relation:

$$A'\left(k_c^2\right) = -2r_L \omega N \frac{(\Pi_{th} + \Pi_v + \Pi_r)}{|P|^2}, \tag{2}$$

$$\widehat{A}\left(k_c^2\right) = \frac{\omega^2}{c_L^2} + \frac{4\pi R_0 N \omega^2}{\omega_0^2 - \omega^2}, \tag{3}$$

where ω_0 and R_0 represent the resonant frequency and the initial radius of the bubble, N is the initial bubble number density and ρ_L is the liquid density. Π_{th}, Π_v, and Π_r stand for heat dissipation, viscous dissipation, and acoustic radiation force dissipation respectively. The radius and the inside pressure of the cavitation bubbles during phase transition process can be simulated based on the Keller-Mikisis equation [32]:

$$\begin{aligned}\rho_L &\left(\left(1 - \frac{1}{c}\frac{dR}{dt}\right) R \cdot \frac{d^2R}{dt^2} + \frac{3}{2}\left(\frac{dR}{dt}\right)^2 \left(1 - \frac{1}{3c}\frac{dR}{dt}\right)\right) \\ &= \left(1 + \frac{1}{c}\frac{dR}{dt} + \frac{R}{c}\frac{d}{dt}\right)\left(P_g + P_V - \frac{2\sigma_L}{R} - 4\frac{\eta_L}{R}\frac{dR}{dt} - P_0 + P_a \sin(\omega t)\right),\end{aligned} \tag{4}$$

where σ_L is the surface tension between the liquid and gas phases, ρ_L represents the liquid density, η_L is the dynamic viscosity of the liquid, R stands for the bubble radius, P_0 and P_a are the static pressure and driving pressure, $\omega = 2\pi f$ is the angular frequency, c is the speed of sound and P_g represents the pressure inside the bubble. Based on the result of the calculated ultrasonic field, the acoustic streaming was simulated by the continuity equation and Navier-Stokes equation [33]:

$$\nabla \cdot U = 0, \tag{5}$$

$$-\nabla \cdot (-Pl + \tau) + \rho_L (U \cdot \nabla) U = F, \tag{6}$$

where U is the flow velocity, τ represents the pressure tensor of viscosity, l stands for the unit matrix and F is the acoustic radiation force per unit volume, which can be calculated by the spatial variation of Reynolds stress. In the model, the no-slip boundary was set in the acoustic streaming module except the surface between the melt and air which was

to be slip boundary. The used physical parameters in simulation were obtained by JMatPro software calculations and references [34,35] as shown in Table 1.

3. Results and discussion

3.1. Acoustic and flow fields inside liquid alloy

The measured stable cavitation intensity I_s and transient cavitation intensity I_t versus solidification time are presented in Fig. 1a and b. Under 14 μm ultrasonic condition, I_t is much less than I_s. As ultrasonic amplitude rises, both I_s and I_t significantly increase and the transient cavitation intensity surpasses the stable cavitation intensity. Once the amplitude attains 18 μm, the average I_s and I_t dramatically increase to the maximum values of 2613 and 3939 W/m^2. The average I_t/I_s ratio shows a remarkable increase with the rise in amplitude, reaching a maximum ratio of 1.5, which indicates that transient cavitation becomes the major energy form during 18 μm ultrasonic solidification. The distribution of acoustic streaming is calculated by Comsol Multiphysics, as displayed in Fig. 1c and d. The acoustic streaming exhibits a simple convective pattern from bottom to top along the center axis, and its rate increases with ultrasonic amplitude. Further statistics indicate that the maximum and average acoustic streaming velocities grow rapidly from 214 to 56 mm/s under 14 μm ultrasonic amplitude to 273 and 71 mm/s under 18 μm ultrasonic amplitude.

3.2. Phase constitution and solidification path

As demonstrated by the X-ray diffraction (XRD) patterns presented in Fig. 2a, the statically solidified alloy sample is comprised of FCC and tetragonal structured phases. Notably, under 14 μm ultrasonic amplitude, the phase remains consistent. However, under ultrasonic amplitudes of 16 and 18 μm, in addition to the FCC and tetragonal phases, a new HCP structure emerges. The DSC curves of the $(FeCoNiCr)_{85}Mo_{15}$ alloy are shown in Fig. 2b. During the heating process, only a single peak appears for the statically solidified alloy sample, indicating that the alloy undergoes a normal eutectic reaction, i.e., L → γ + σ. Under 14 μm ultrasonic amplitude, the melting process and solidification path are similar to those under static condition. As the amplitude rises to 16 and 18 μm, several endothermic peaks emerge in the heating curves, suggesting that there are other phase transition processes, in addition to the original eutectic reaction.

3.3. Stable (γ+σ) eutectic structure modulated by power ultrasounds

3.3.1. Eutectic morphology transition

The solidified (γ+σ) eutectic structures under different ultrasonic conditions are shown in Fig. 3. After static solidification, well-developed fishbone-like eutectic structure consisting of lamellar γ and σ phases forms. The EDS analysis reveals that the contents of γ phase are 23.3 at.% Ni, 22.6 at.% Fe, 22.1 at.% Co, 19.6 at.% Cr, and 12.4 at.% Mo, and the σ phase exhibits 23.8 at.% Mo, 21.1 at.% Cr, 19.8 at.% Fe, 19.6 at.% Co, and 15.7 at.% Ni. When 14 and 16 μm ultrasounds are applied, the regular eutectic undergoes great refinement, with lamellar spacing sharply decreasing from 1.4 μm during static solidification to 0.4 μm under 16 μm ultrasonic amplitude. Based on the published reports [36] and our previous work, the phenomenon of eutectic refinement can be ascribed to two primary factors. Firstly, stable cavitation dominating the cavitation effect under ultrasound condition with small amplitudes improves wettability by decreasing the contact angle between impurity particles and the molten alloy, thereby facilitating heterogeneous nucleation and resulting in the refinement of eutectic cells. Secondly, according to the J-H model [37], the lamellar spacing is inversely proportional to the growth rate of the eutectic. Therefore, the acoustic streaming accelerates the growth rate of the eutectic by reducing accumulation and enlarges the solute gradient at the front of solid-liquid interface, which further promotes the refinement of the lamellar spacing.

Table 1
Physical parameters used to calculate acoustic and flow fields.

Parameters	Units	Value	References
Ultrasound source frequency, f	kHz	20	Self setting
Density of liquid alloy, ρ_L	kg/m^3	7595	[34]
Surface tension of liquid alloy, σ_L	N/m	1.29	[34]
Viscosity of liquid alloy, η_L	10^{-3} Pa s	4.0	[34]
Sound speed, c_L	m/s	5000	[35]
Sound speed in graphite mold, c_m	m/s	3000	[35]
Displacement from ultrasonic horn, A	μm	14, 16, 18	This work

However, when ultrasonic amplitude goes up to 18 μm, the regular eutectic only accounts for 19.6 % volume fraction of the microstructure, displaying coarsened lamellar spacing of 2 μm (Fig. 4a). Meanwhile, anomalous eutectic becomes the major morphology form, whose volume fraction further increases with the rise of ultrasonic amplitude. These phenomena are attributed to the local high-pressure induced by transient cavitation, which is described by the following Clausius-Clapeyron equation [38]:

$$\Delta T_p = \frac{T_L \Delta V}{\Delta H} \Delta P, \tag{7}$$

where ΔT_p respects the undercooling generated by sound pressure; T_L is the liquidus temperature; ΔP is the relative sound pressure; ΔV and ΔH are the volume change and enthalpy change during solidification of the alloy, respectively. Therefore, the pressure generated by cavitation has an impact on the nucleation rate by changing local undercoolings. According to the classical theory of nucleation [39], the nucleation rate J reads

$$J = J_0 \cdot \exp\left(-\frac{\Delta G^*}{k_B T}\right) \cdot \exp\left(-\frac{Q}{k_B T}\right), \tag{8}$$

$$\Delta G^* = \frac{16\pi\sigma^3 T_L^2}{3\Delta H_m{}^2 \Delta T^2} f(\theta), \tag{9}$$

$$\sigma = \frac{\alpha_m \Delta H_m}{\left(N V_m^2\right)^{\frac{1}{3}}}, \tag{10}$$

where J_0 is the nucleation factor usually taken as 10^{41} m^{-3} s^{-1}; Q is the activation energy for atomic diffusion, and exp(-Q/k_BT) is set to 10^{-2} due to little change of Q with temperature [40]; θ is the contact angle between alloy melt and the solid impurity; σ is the liquid-solid interface energy; α_m is the factor of structural difference between crystalline and liquid taken as 0.86 for FCC crystal and 0.48 for Tetragonal crystal; ΔH_m is latent heat, which is obtained from DSC curves; V_m is the molar volume; N is the Avogadro constant. The parameters used are calculated by CALPHAD software and obtained from Ref. [35], as listed in Table 2.

The nucleation rate variation with the pressure is drawn in Fig. 4c. Clearly, the local high-pressure induced by transient cavitation under high ultrasonic amplitude markedly amplifies the disparity in nucleation rates between the two phases, ultimately leading to their independent nucleation. Subsequently, the intense acoustic streaming generated during the early stages of solidification, which extends the diffusion distance of constituent elements to maintain the γ and σ phases independent growth for anomalous eutectic. In the late solidification period, the transient cavitation intensity decreases, which no longer leads to independently nucleate for γ and σ phases, while the prolonged diffusion distance causes the lamellar coarsening of the eutectic formed through dependent nucleation and growth. Consequently, γ phase grows as the leading phase during anomalous eutectic formation due to more independent nuclei, which results in its volume fraction increasing from 44.0 % to 62.6 % within the whole (γ+σ) eutectic structure, and that of σ phase steadily decreasing from 56.0 % to 30.8 % (Fig. 4b).

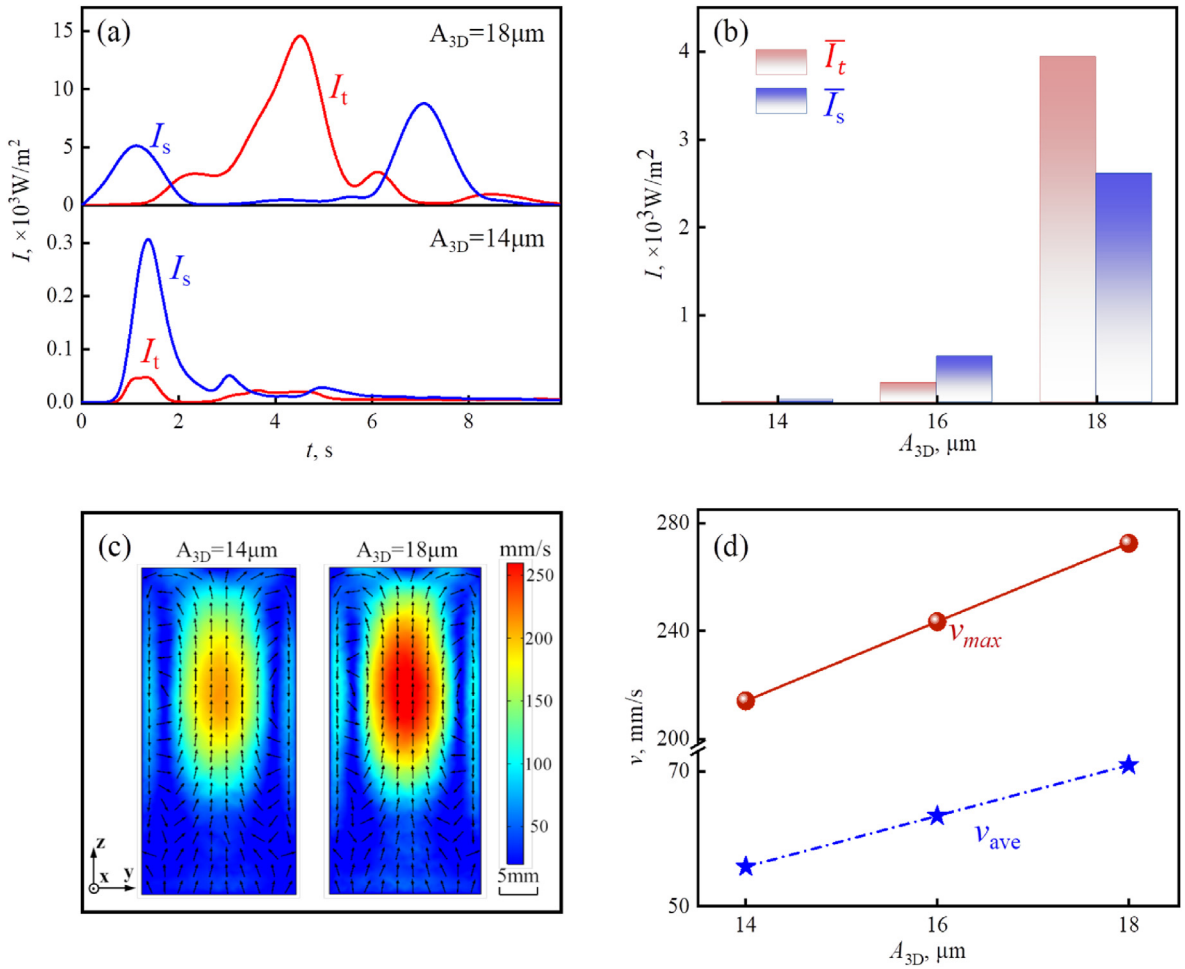

Fig. 1. Acoustic field and flow field characteristics inside solidifying $(FeCoNiCr)_{85}Mo_{15}$ alloy: (a) measured stable and transient cavitation intensity; (b) average stable and transient cavitation intensities; (c) calculated flow field distribution; (d) average and maximum velocities of acoustic streaming versus 3D ultrasonic amplitude.

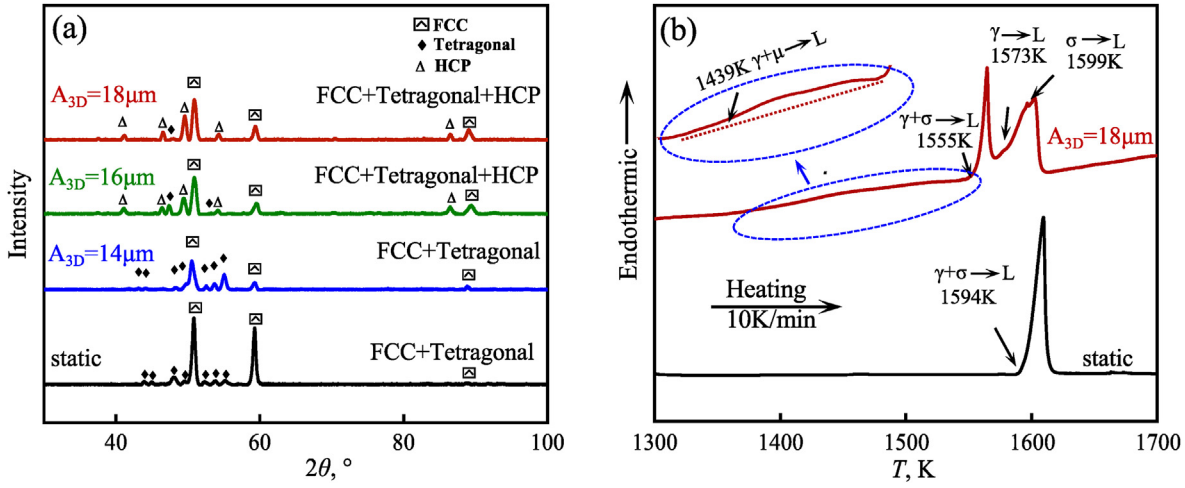

Fig. 2. Phase constitution and thermal analysis of $(FeCoNiCr)_{85}Mo_{15}$ alloy solidified under different ultrasonic conditions: (a) XRD patterns; (b) DSC melting curve.

3.3.2. *Interphase orientation transition*

Fig. 5 illustrates the orientation relationship of the γ/σ interfaces under static (Fig. 5a) and 14 μm ultrasonic (Fig. 5b) conditions. The bright field image captured under static condition combined with high-resolution imaging at the γ/σ interface and corresponding fast Fourier transform (FFT) images, indicate a semi-coherent interface orientation characterized by $[001]_\gamma//[112]_\sigma$ and $(-110)_\gamma//(11\text{-}1)_\sigma$ relationships. Magnified structural images (Fig. 5a_3 and a_4) reveal that the FCC-structured γ phase has a lattice parameter of $a_\gamma = 0.372$ nm, and the tetragonal σ phase exhibits lattice constants of $a_\sigma = 0.908$ nm and $c_\sigma = 0.444$ nm. Under the application of 14 μm ultrasounds, the γ phase's lattice constant (a_γ) decreases slightly to 0.369 nm, and that of tetragonal

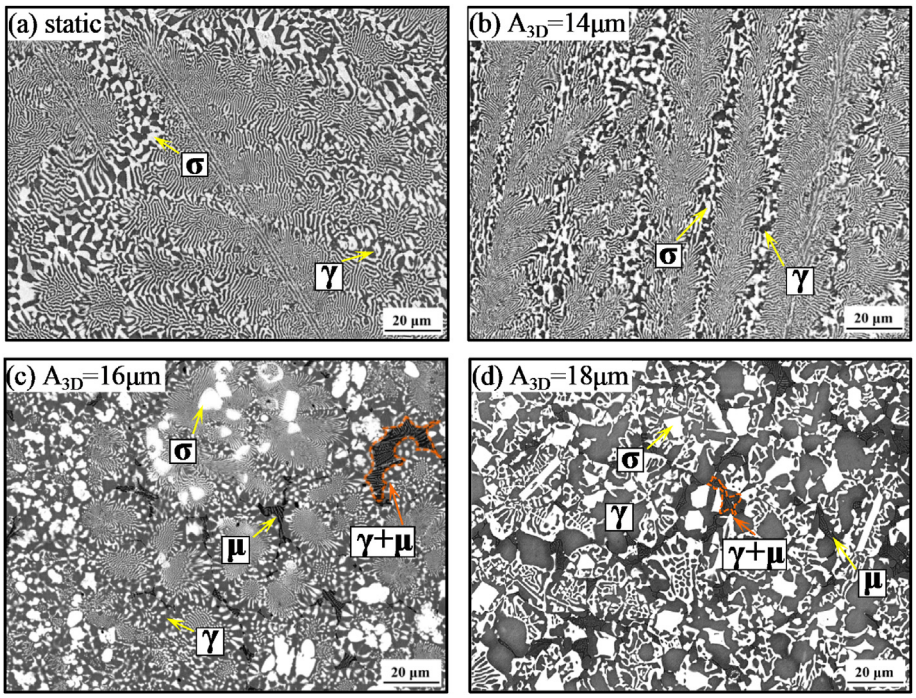

Fig. 3. Ultrasonic solidification microstructure of $(FeCoNiCr)_{85}Mo_{15}$ alloy: (a) static; (b) 14 μm ultrasonic amplitude; (c) 16 μm ultrasonic amplitude; (d) 18 μm ultrasonic amplitude.

σ phase increases to $a_\sigma = 0.911$ nm and $c_\sigma = 0.482$ nm. Importantly, the γ/σ interface relationship undergoes a complete alternation, characterized by the alignment of $[011]_\gamma//[-110]_\sigma$ and $(-11\text{-}1)_\gamma//(001)_\sigma$. Fig. 5$a_6$ and b_6 show the crystalline structures corresponding to the orientation relationships for the regular eutectic under static and 14 μm ultrasonic conditions, respectively. The presence of common lattice atoms of γ and σ phases represented by yellow spheres illustrates that the phase boundaries retain semi-coherent.

Fig. 6 shows more extensive analyses using EBSD, revealing the statistical crystallographic orientation between γ and σ phases under different conditions. Judged by the orientation relationship (OR) boundary map and pole figures, the lamellar eutectic interfaces in the static sample exhibit less than 5° misorientation, which well fits the semi-coherent relationship of $[001]_\gamma//[112]_\sigma$ and $(-110)_\gamma//(11\text{-}1)_\sigma$ (Fig. 6a and b). As for the 14 μm ultrasonic sample (Fig. 6d and e), the γ/σ interface relationship not only is alternated to $[011]_\gamma//[-110]_\sigma$ and $(-11\text{-}1)_\gamma//(001)_\sigma$ but also has a higher proportion of strictly semi-coherent interfaces. This confirms that the crystallographic orientation transformation induced by ultrasound is complete, rather than partial.

According to thermodynamic theory [41], eutectic phases generally grow in a synergistic manner, with the interface orientation aligning in a way that corresponds to the lower energy state. This alignment generally occurs when the coherent crystal planes of the two phases coincide with their respective close-packed planes. The close-packed planes for FCC, BCC, hexagonal close-packed (HCP), and tetragonal structures are {111}, {011}, {0001}, and {001} respectively [42,43]. A well-known example is the K-S relationship, where the {111} plane of the FCC structure is coherent with the {011} plane of the BCC structure [44]. However, in the actual solidification process, not all eutectic interfaces adopt the lowest energy configuration. In the present work, the statically solidified $(FeCoNiCr)_{85}Mo_{15}$ alloy sample exhibits the semi-coherent interface orientation rather than the most stable configuration. When 14 μm ultrasounds are applied, high-frequency vibration provides additional activation energy and facilitates the alternation of the interface relationship into a lower-energy state, leading to the γ phase with FCC structure and the σ phase with tetragonal structure growing synergistically along their close-packed planes to form the most stable crystal orientation relationship.

3.3.3. *Crystalline structure variation of σ phase*

With the further rise of ultrasonic amplitude, σ phase structure unexpectedly transforms from tetragonal to HCP structure thoroughly, as shown by the TEM and EBSD analysis of 18 μm ultrasounds specimen in Fig. 7. The lattice parameters of the HCP-structured σ phase are $a_\sigma = 0.771$ nm and $c_\sigma = 1.950$ nm, and the γ phase maintains its FCC structure with a lattice constant of $a_\gamma = 0.369$ nm as determined by the TEM results in Fig. 7a_2-a_4.

Utilizing the above crystallographic information, more comprehensive regional analysis can be conducted using EBSD. As demonstrated in Fig. 7b_1, the EBSD phase mapping further confirms that the structure of σ phase in both the regular and anomalous eutectic completely transforms into HCP. In the regular eutectic part, the γ/σ interface still exhibits a semi-coherent relationship, while the specific orientation relationship alters to $[011]_\gamma//[-1-120]_\sigma$, $(-11-1)_\gamma//(1\text{–}101)_\sigma$, where the parallel planes correspond to their respective close-packed planes, representing the most stable configuration in this case. In the OR boundary map (Fig. 7b_2), 5° is taken as the threshold to determine whether the designated crystallographic orientations are parallel to each other. The blue boundary lines further show that the semi-coherent orientation relationship exists only in the regular eutectic region (Fig. 7b_2). In contrast, within the anomalous eutectic region, the γ/σ interface lacks any crystallographic correlation. The above structural transformation may be related to the local high-pressure nucleation environment caused by intensive transient cavitation.

3.4. *Metastable (γ+μ) eutectic formation induced by ultrasounds*

When ultrasonic amplitude exceeds 16 μm, a small amount of metastable (γ+μ) eutectic structure unexpectedly appears among stable (γ+σ) eutectic cells, as shown in Fig. 3c and d. SAED patterns of the eutectic structure (Fig. 8b and c) indicate that μ phase adopts a tetragonal structure with lattice constants of $a_\mu = 1.443$ nm and $c_\mu = 0.801$ nm. Furthermore, the FFT image at the γ/μ interface displays the semi-coherent relationship of $[011]_\gamma//[211]_\mu$, and $(-11-1)_\gamma//(-11-1)_\mu$, as

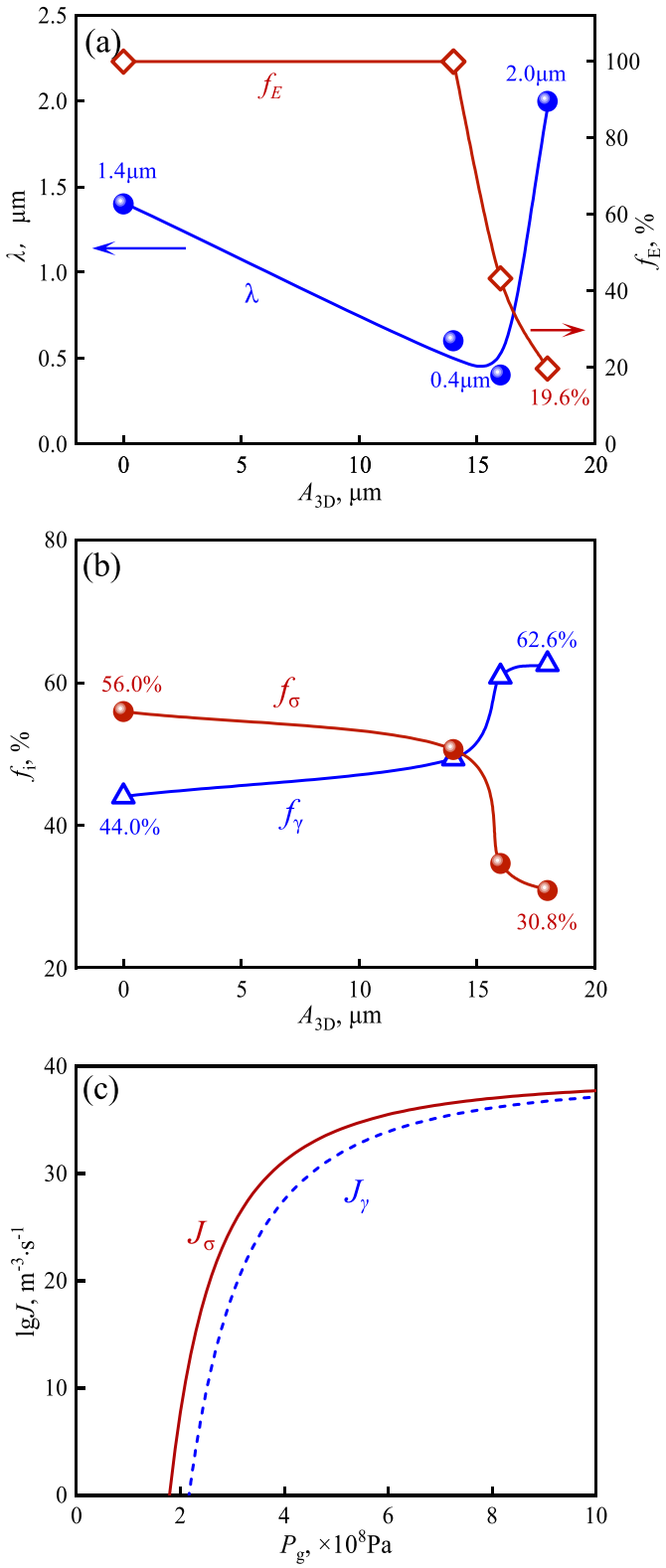

Fig. 4. The (γ+σ) eutectic characteristics versus 3D ultrasonic amplitude: (a) interlamellar spacing and eutectic volume fraction; (b) volume fractions of γ and σ phases; (c) the ultrasonic cavitation effect on the nucleation rates of γ and σ phases.

depicted in Fig. 8d. EDS-mapping results for the (γ+μ) eutectic region (Fig. 8e) reveal its composition of 35.3 at.% Cr, 23.5 at.% Fe, 21.4 at.% Co, 12.6 at.% Ni, and 7.2 at.% Mo. The μ phase is enriched in Cr element,

Table 2
Physical parameters used in the calculation of nucleation rates.

Parameters	Units	Values	Reference
Molar enthalpy change of σ phase, ΔH_m^σ	J/mol	1.65×10^4	This work
Molar enthalpy change of γ phase, ΔH_m^γ	J/mol	1.41×10^4	This work
Volume change of alloy during solidification, ΔV	%	3.83	[35]
Fusion enthalpy of alloy, ΔH	J/m^3	1.13×10^9	This work
Liquidus temperature, T_L	K	1613	This work
Wetting angle factor, $f(\theta)$	–	0.0001	Self setting

with a content up to 47.0 at.%, while the γ phase is enriched in Fe, Co, and Ni, with concentrations of 27.5 at.%, 28.5 at.%, and 25.5 at.%, respectively.

Under the effect of strong acoustic streaming within 3D ultrasounds fields, the (γ+μ) eutectic region contains the Cr concentration of 35.3 at.%, which is greater than the average concentration. Based on the solute distribution data alongside statistical analysis, a thermodynamic pseudo-binary phase diagram for the $(Fe_{23.5}Co_{21.4}Ni_{12.6}Mo_{7.2})_{100-x}Cr_x$ alloy is constructed by CALPHAD software, as shown in Fig. 8f. It assumes that the solute composition in the examined (γ+μ) eutectic region is approaching that in remaining liquid, suggesting that the concentration of residual liquid is close to the predicted eutectic point of 40.5 at.% Cr. As the temperature decreases, the Cr-rich μ phase and γ phase simultaneously nucleate and grow into the lamellar eutectic structure from the residual liquid alloy. In fact, our previous work has demonstrated that in the $FeCoCrNi_{2.1}Al$ system, intense acoustic streaming generated by the ultrasound could promote the diffusion of Cr from the solid-liquid interface into the liquid phase [28], causing Cr atoms to accumulate in the remaining liquid and ultimately promoting the precipitation of Cr-rich metastable phase.

3.5. Ultrasounds enhanced synergy of strength and plasticity

Fig. 9a displays the compressive strength-strain curves for $(FeCoNiCr)_{85}Mo_{15}$ alloy solidified under static and ultrasonic conditions. The yield strength, compressive strength, and strain for statically solidified alloy sample are 1400 MPa, 1774 MPa and 10.28 %, respectively. When ultrasonic amplitude is 14 μm, yield strength and compressive strength both rapidly increase to 2000 and 2197 MPa with unchanged ductility. As the ultrasonic amplitude increases to 18 μm, the ductility elevates by more than 2 times to 21.4 %. The yield strength-strain comparison between $(FeCoNiCr)_{85}Mo_{15}$ alloy in this work and other Mo-containing alloys reported in Refs. [9–11,45–52] is drawn in Fig. 9b. The ultrasonically solidified $(FeCoNiCr)_{85}Mo_{15}$ alloy shows obvious superiority in both strength and plasticity than other Mo containing alloys. Through the design of 3D ultrasounds, both strength and plasticity can be actively modulated in a wide range over their trade-off effect.

The Schmid Factor (SF) is generally used to reflect the feasibility and extent of activation of a particular slip system under a given loading direction [53]. The smaller the SF value, the more difficult it is to activate the slip system, and correspondingly, the greater the stress that can be sustained [54]. Based on the EBSD orientation data, the SF distribution maps for the slip systems under static condition of $\{-110\}_\gamma <001>_\gamma$ and $\{11-1\}_\sigma <112>_\sigma$, as well as under 14 μm ultrasounds condition of $\{-11-1\}_\gamma <011>_\gamma$ and $\{001\}_\sigma <-110>_\sigma$, are shown in Fig. 10a and b. Clearly, compared with that of statically solidified alloy sample, the SF value under 14 μm ultrasounds is smaller, indicating that the activation of the slip system is more difficult. Therefore, the alteration of crystallographic orientation relationship of γ/σ phase interfaces contributes to the improvement of yield strength through increasing resistance to dislocation motion. Moreover, the increase in the number of interfaces between the γ and σ phases brought by the refinement of eutectic lamellae, not only impedes dislocation movement but also promotes the

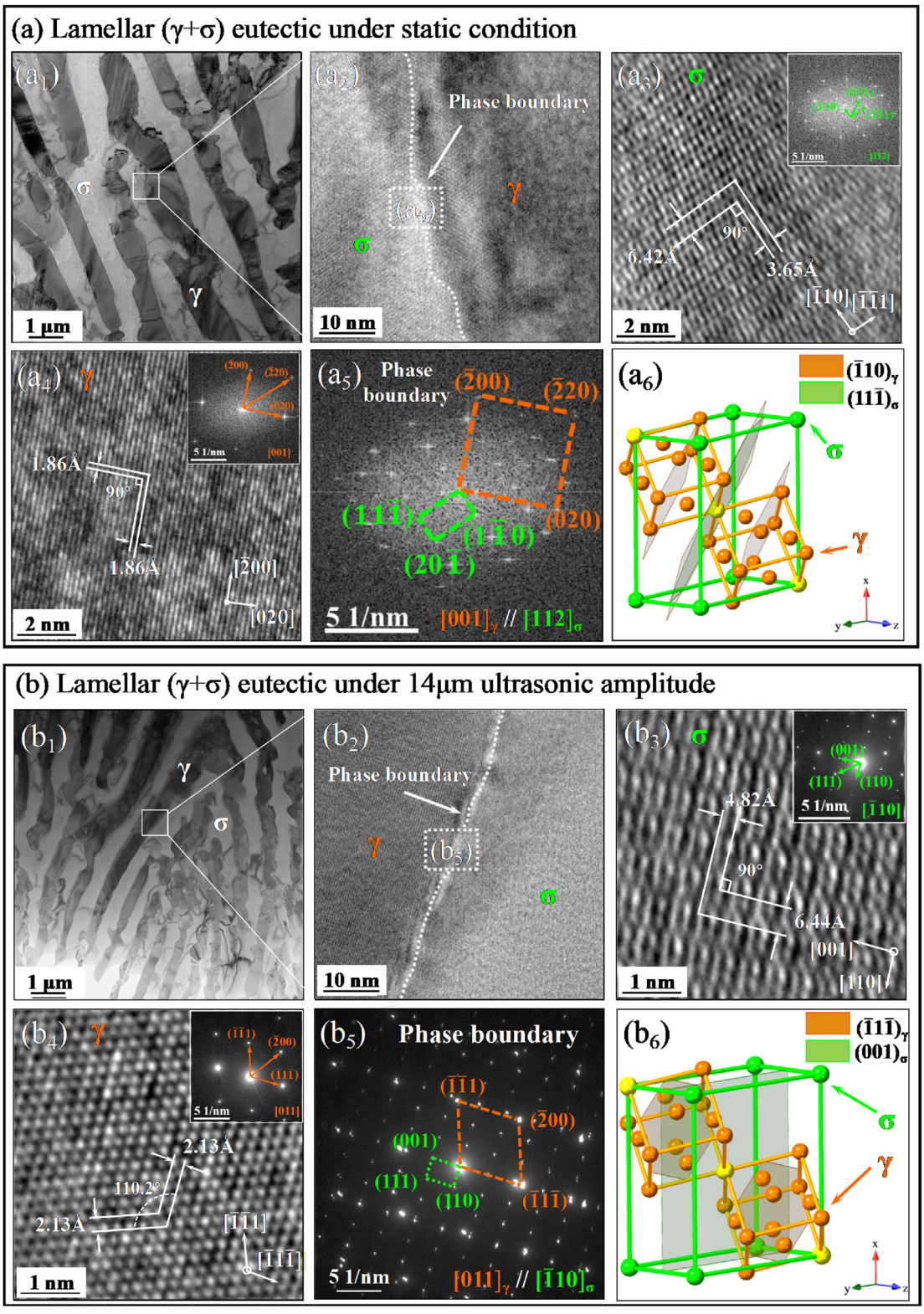

Fig. 5. Interface orientation of lamellar (γ+σ) eutectic structures: (a) static solidification and (b) 14 μm ultrasonic amplitude; (a_1) and (b_1) bright field images; (a_2) and (b_2) HRTEM images of σ/γ interface; (a_3) and (b_3) HRTEM images of σ phase and (a_4) and (b_4) HRTEM images of γ phase; (a_5) and (b_5) FFT/SAED images of σ/γ interface; (a_6) and (b_6) visualization of the semi-coherent interface.

generation of back stress [55]. Thereby strain-hardening capability is enhanced, jointly leading to the remarkable improvement of yield strength and ultimate strength.

The main reasons for the enhancement of ductility under 16 and 18 μm ultrasonic solidification conditions mainly come from two aspects. Firstly, the remarkable γ phase volume fraction increase from 44.0 % to 62.6 % provides sufficient space for dislocation motion, which might be the most critical factor for the ductility enhancement. Secondly, the crystallographic structure of σ phase transitions from tetragonal to HCP structure, which brings great symmetry and higher packing density,

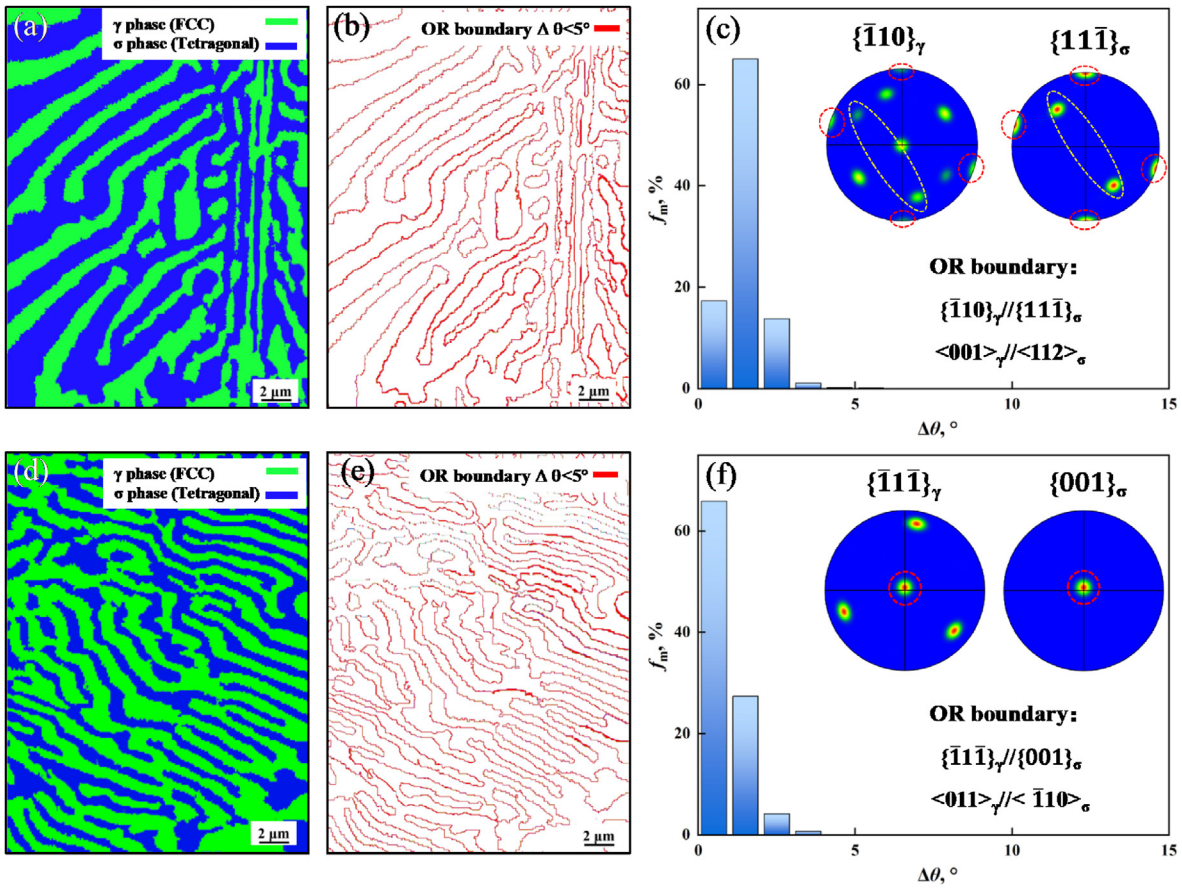

Fig. 6. EBSD analysis of lamellar (γ+σ) eutectic structures: (a) the phase mapping, (b) boundary mapping, and (c) pole figures with the interface misorientation distribution of static sample; (d) the phase mapping, (e) boundary mapping, and (f) pole figures with the interface misorientation distribution of 14 μm ultrasonic sample.

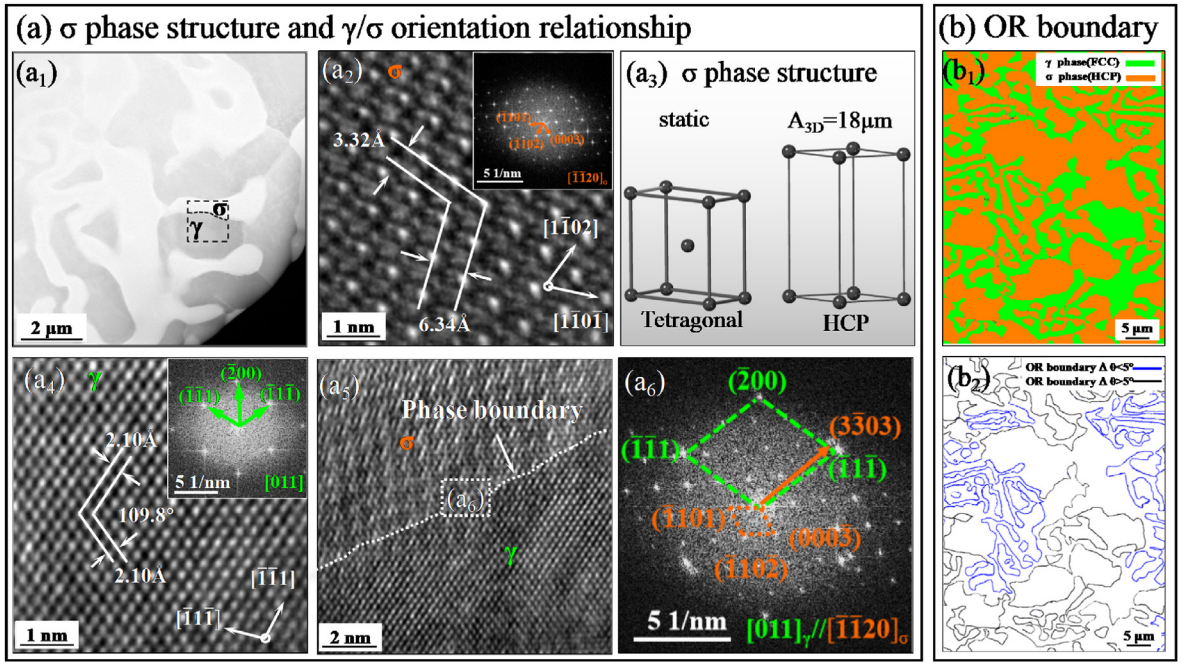

Fig. 7. The *σ* phase crystal structure and orientation relationship in (γ+σ) eutectic structures under 18 μm ultrasonic amplitude: (a) TEM characterization; (a_1) HAADF image; (a_2) HRTEM images with FFT of σ phase; (a_3) structure transformation of σ phase; (a_4) HRTEM image with FFT of γ phase; (a_5) HRTEM and (a_6) FFT image of σ/γ interface; (b) EBSD analysis, (b_1) phase mapping, and (b_2) phase boundary distribution.

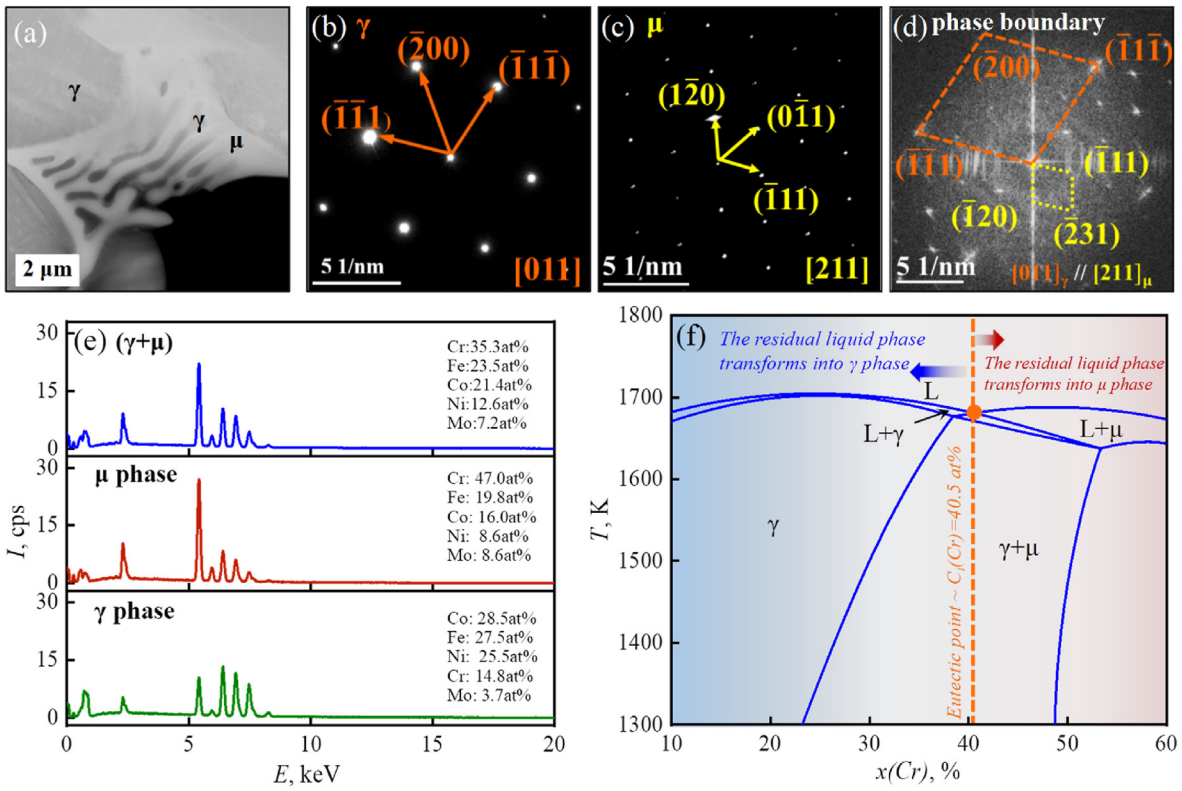

Fig. 8. Crystallographic and compositional characteristics of (γ+μ) eutectic structures: (a) HADDF image; (b) SAED image for γ phase, (c) SAED image for μ phase; (d) FFT image at γ/μ interface; (e) phase composition; (f) the pseudo-binary phase diagram of $(Fe_{23.5}Co_{21.4}Ni_{12.6}Mo_{7.2})_{100-x}Cr_x$ alloy calculated by CALPHAD based on the composition of (γ+μ) eutectic region.

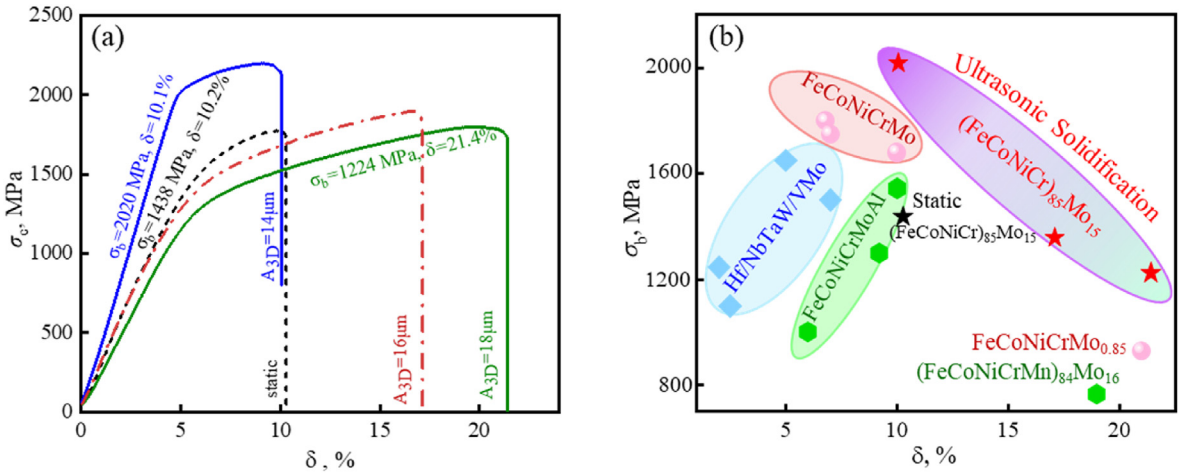

Fig. 9. Compressive property of $(FeCoNiCr)_{85}Mo_{15}$ alloy: (a) strength-strain curves of statically and ultrasonically solidified alloy samples; (b) the "yield strength-strain" comparison between this work and as-solidified alloys containing Mo element.

leading to strong atomic interactions to withstand deformation. In addition, a limited quantity of newly developed (γ+μ) regular eutectics featuring semi-coherent interfaces could facilitate the coordination of deformation between the block γ and σ phases in anomalous eutectic region, which serves to mitigate stress concentration and postpone the fracture of the alloy, thereby improving the ductility.

4. Conclusions

The eutectic microstructure transition and corresponding mechanical property improvement for multicomponent $(FeCoNiCr)_{85}Mo_{15}$ alloy were studied under 3D ultrasounds. The main conclusions are summarized as follows.

(1) Under weak ultrasounds condition, the stable (γ+σ) lamellar eutectic structures exhibited significant refinement, and the high frequency vibration induced by ultrasound shifted the γ/σ interface orientation from $[001]_\gamma//[112]_\sigma$ and $(-110)_\gamma//(11-1)_\sigma$ to the most stable configuration of $[011]_\gamma//[-110]_\sigma$ and $(-11-1)_\gamma//(001)_\sigma$.

(2) Under the intensive transient cavitation effect generated by strong ultrasounds, the lamellar eutectic predominantly evolved into

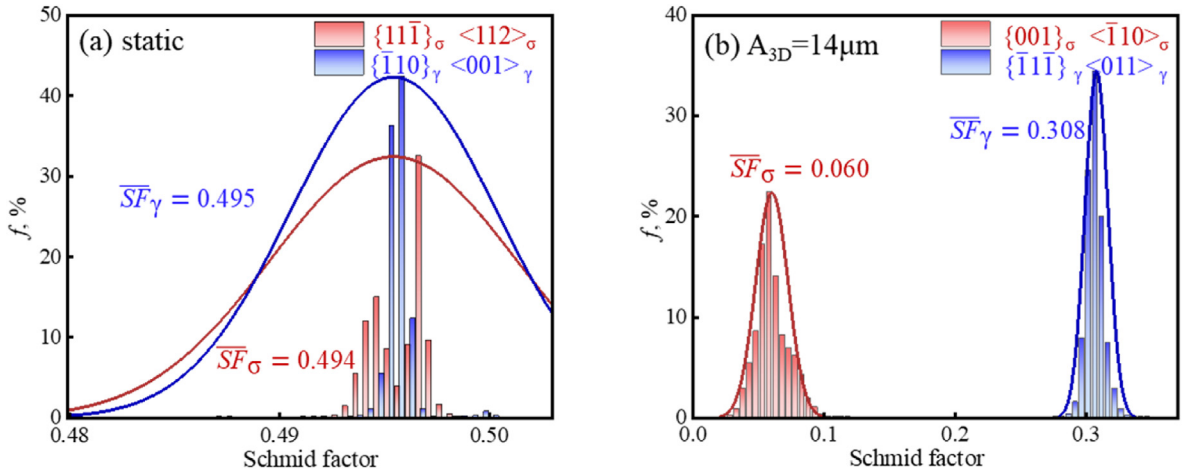

Fig. 10. Schmid factor distribution for slip modes of $(FeCoNiCr)_{85}Mo_{15}$ alloy under different conditions: (a) static solidification; (b) 14 μm ultrasonic amplitude.

anomalous eutectic accompanied with the complete crystallographic transformation of σ phase from tetragonal to HCP structure. The intensive acoustic streaming induced by ultrasounds promoted the diffusion of Cr element during γ phase growth, which caused the residual liquid composition approaching eutectic point and stimulated the formation of a novel metastable (γ+μ) eutectic with the semi-coherent relationship $[011]_\gamma//[211]_\mu$ and $(-11-1)_\gamma//(-11-1)_\mu$.

(3) The maximum yield strength, ultimate strength, and alloy ductility after ultrasonic solidification attained 2000 MPa, 2197 MPa, and 21.4 %, which corresponded to increases by 1.4, 1.2, and 2.1 times in comparison with those of statically solidified alloys. Both strength and plasticity are actively modulated in a wide range over their trade-off effect by 3D ultrasounds.

(4) The enhancement of strength is mainly attributed to the stable interface configuration facilitated by weak ultrasounds and the refinement of stable (γ+σ) lamellar eutectics. The significant volume fraction increase of FCC-structured γ phase and the crystallographic transformation of σ phase into HCP structure induced by strong ultrasounds jointly improved alloy ductility.

CRediT authorship contribution statement

W.J. Gao: Writing – original draft, Investigation, Formal analysis, Data curation. **X. Wang:** Writing – review & editing, Validation, Investigation, Formal analysis. **J.Y. Wang:** Resources, Funding acquisition. **W. Zhai:** Writing – review & editing, Resources, Methodology, Funding acquisition, Conceptualization. **B. Wei:** Writing – review & editing, Resources, Funding acquisition, Conceptualization.

Declaration of competing interest

The authors declare that they have no known competing financial interests or personal relationships that could have appeared to influence the work reported in this paper.

Acknowledgements

This work was financially supported by the National Natural Science Foundation of China (Nos. 52130405, 52088101, U24A20206), Research Plan of Shaanxi Province (No. 2023-JC-JQ-28, 2024ZY-JCYJ-04-07). The authors are very grateful to Meimei Zhao and Hong Li for their technical assistance.

References

[1] Y.P. Lu, X.Z. Gao, J. Li, Z.N. Chen, T.M. Wang, J.C. Jie, H.J. Kang, Y.B. Zhang, S. Guo, H.H. Ruan, Y.H. Zhao, Z.Q. Cao, T.J. Li, Directly cast bulk eutectic and near-eutectic high entropy alloys with balanced strength and ductility in a wide temperature range, Acta Mater. 124 (2017) 143–150, https://doi.org/10.1016/j.actamat.2016.11.016.

[2] J.M. Rickman, H.M. Chan, M.P. Harmer, J.A. Smeltzer, C.J. Marvel, A. Roy, G. Balasubramanian, Materials informatics for the screening of multi-principal elements and high-entropy alloys, Nat. Commun. 10 (1) (2019) 2618, https://doi.org/10.1038/S41467-019-10533-1.

[3] Q.F. Wu, Z.J. Wang, X.B. Hu, T. Zheng, Z.S. Yang, F. He, J.J. Li, J.C. Wang, Uncovering the eutectics design by machine learning in the Al-Co-Cr-Fe-Ni high entropy system, Acta Mater. 182 (2020) 278–286, https://doi.org/10.1016/j.actamat.2019.10.043.

[4] J. Charkhchian, A. Zarei-Hanzaki, A. Moshiri, H.R. Abedi, T.M. Schwarz, R. Lawitzki, G. Schmitz, K. Chadha, C. Aranas Jr., J.J. Shen, J.P. Oliveira, Spinodal decomposition of B2-phase and formation of Cr-rich nano-precipitates in $AlCoCrFeNi_{2.1}$ eutectic high-entropy alloy, Adv. Eng. Mater. 25 (2023) 2300164, https://doi.org/10.1002/adem.202300164.

[5] M. Abdullah, M. Mukarram, T.B. Yaqub, F. Fernandes, K. Yaqub, Development of eutectic high entropy alloy by addition of W to CoCrFeNi HEA, Int. J. Refractory Met. H. 115 (2023) 106300, https://doi.org/10.1016/j.ijrmhm.2023.106300.

[6] B. Chanda, S.K. Pani, J. Das, Mechanism of microstructure evolution and spheroidization in ultrafine lamellar $CoCrFeNi(Nb_{0.5}/Ta_{0.4})$ eutectic high entropy alloys upon hot deformation, Mater. Sci. Eng. 835 (2022) 142669, https://doi.org/10.1016/j.msea.2022.142669.

[7] S.A. Krishna, N. Noble, N. Radhika, B. Saleh, A comprehensive review on advances in high entropy alloys: fabrication and surface modification methods, properties, applications, and future prospects, J. Manuf. Process. 109 (2024) 583–606, https://doi.org/10.1016/j.jmapro.2023.12.039.

[8] M. Mukarram, M. Mujahid, K. Yaqoob, Design and development of CoCrFeNiTa eutectic high entropy alloys, J. Mater. Res. Technol. 10 (2021) 1243–1249, https://doi.org/10.1016/j.jmrt.2020.12.042.

[9] Y. Guo, L. Liu, Y. Zhang, J.G. Qi, B. Wang, Z.F. Zhao, J. Shang, J. Xiang, A superfine eutectic microstructure and the mechanical properties of $CoCrFeNiMo_x$ high-entropy alloys, J. Mater. Res. 33 (2018) 3258–3265, https://doi.org/10.1557/jmr.2018.177.

[10] T.T. Shun, L.Y. Chang, M.H. Shiu, Microstructure and mechanical properties of multiprincipal component $CoCrFeNiMo_x$ alloys, Mater. Char. 70 (2012) 63–67, https://doi.org/10.1016/j.matchar.2012.05.005.

[11] Y. Liu, Y.X. Xie, S.G. Cui, Y.L. Yi, X.W. Xing, X.J. Wang, W. Li, Effect of Mo element on the mechanical properties and tribological responses of $CoCrFeNiMo_x$ high-entropy alloys, Metals 11 (2021) 486, https://doi.org/10.3390/met11030486.

[12] C. Schulz, A. Kauffmann, S. Laube, M. Kellner, B. Nestler, M. Heilmaier, Role of orientation relationship for the formation of morphology and preferred orientation in NiAl-(Cr,Mo) during directional solidification, Acta Mater. 231 (2022) 117857, https://doi.org/10.1016/j.actamat.2022.117857.

[13] M.L. Wang, Y.P. Lu, J.G. Lan, T.M. Wang, C. Zhang, Z.Q. Cao, T.J. Li, P.K. Liaw, Lightweight, ultrastrong and high thermal-stable eutectic high-entropy alloys for elevated-temperature applications, Acta Mater. 248 (2023) 118806, https://doi.org/10.1016/j.actamat.2023.118806.

[14] G.R. Lindemann, P. Chao, V. Nikitin, V. De Andrade, M. De Graef, Complexity and evolution of a three-phase eutectic during coarsening uncovered by 4D nano-imaging, Acta Mater. 266 (2024) 119684, https://doi.org/10.1016/j.actamat.2024.119684.

[15] Y. Wang, W. Chen, J. Zhang, J. Zhou, A quantitative understanding on the mechanical behavior of AlCoCrFeNi$_{2.1}$ eutectic high-entropy alloy, J. Alloys Compd. 850 (2021) 156610, https://doi.org/10.1016/j.jallcom.2020.156610.

[16] A. Priyadarshi, M. Khavari, T. Subroto, M. Conte, P. Prentice, K. Pericleous, D. Eskin, J. Durodola, I. Tzanakis, On the governing fragmentation mechanism of primary intermetallics by induced cavitation, Ultrason. Sonochem. 70 (2021) 105260, https://doi.org/10.1016/j.ultsonch.2020.105260.

[17] Y. Yao, Y. Pan, S.Q. Liu, Power ultrasound and its applications: a state-of-the-art review, Ultrason. Sonochem. 62 (2020) 104722, https://doi.org/10.1016/j.ultsonch.2019.104722.

[18] Y.J. Hu, J.Y. Wang, N.X. Xu, W. Zhai, B. Wei, Three orthogonally arranged ultrasounds modulate solidification microstructures and mechanical properties for AZ91 magnesium alloy, Acta Mater. 241 (2022) 118382, https://doi.org/10.1016/j.actamat.2022.118382.

[19] S.B. Kim, Y.H. Cho, J.M. Lee, J.G. Jung, Y.K. Lee, Combined effects of ultrasonic melt treatment and Cu/Mg solute on the microstructure and mechanical properties of a hypoeutectic Al-7Si alloy, Metall. Mater. Trans. A 50 (2019) 1534–1544, https://doi.org/10.1007/s11661-018-5069-2.

[20] W. Zhai, X. Lu, B. Wei, Microstructural evolution of ternary $Ag_{33}Cu_{42}Ge_{25}$ eutectic alloy inside ultrasonic field, Prog. Nat. Sci. 24 (2014) 642–648, https://doi.org/10.1016/j.pnsc.2014.10.010.

[21] G.I. Eskin, D.G. Eskin, Ultrasonic Treatment of Light Alloy Melts, CRC Press, Boca Raton, 2015.

[22] Y.J. Hu, J.Y. Wang, W. Zhai, B. Wei, Ultrasounds induced microstructure transition and improved mechanical property of directionally solidified ternary Cu-Al-Ni alloy, Metall. Mater. Trans. B 55 (2024) 3736–3749, https://doi.org/10.1007/s11663-024-03213-z.

[23] C.J. Todaro, M.A. Easton, D. Qiu, D. Zhang, M.J. Bermingham, E.W. Lui, M. Brandt, D.H. StJohn, M. Qian, Grain structure control during metal 3D printing by high-intensity ultrasound, Nat. Commun. 11 (2020) 142, https://doi.org/10.1038/s41467-019-13874-z.

[24] X. Wang, J.Y. Wang, R.H. Xiao, W. Zhai, B. Wei, Modulating phase constitution and copper microsegregation for FeCoNiCuAl high-entropy alloy by optimized ultrasonic solidification, Metall. Mater. Trans. A 55 (2024) 4330–4341, https://doi.org/10.1007/s11661-024-07581-8.

[25] J.G. Jung, Y.H. Cho, S.D. Kim, S.H. Lee, K. Song, K. Euh, J.M. Lee, Mechanism of ultrasound-induced microstructure modification in Al–Zr alloys, Acta Mater. 199 (2020) 73–84, https://doi.org/10.1016/j.actamat.2020.08.025.

[26] J.M. Liu, W. Zhai, B.J. Wang, X. Ma, P.X. Yan, B. Wei, Structure and property modulation of primary CoSn and peritectic $CoSn_2$ intermetallic compounds through ultrasonicating liquid Sn–10%Co alloy, J. Alloys Compd. 827 (2020) 154297, https://doi.org/10.1016/j.jallcom.2020.154297.

[27] S. Chankitmunkong, D.G. Eskin, C. Limmaneevichitr, Structure refinement, mechanical properties and feasibility of deformation of hypereutectic Al-Fe-Zr and Al-Ni-Zr alloys subjected to ultrasonic melt processing, Mater. Sci. Eng. A 788 (2020) 139567, https://doi.org/10.1016/j.msea.2020.139567.

[28] X. Wang, W. Zhai, H. Li, J.Y. Wang, B. Wei, Ultrasounds induced eutectic structure transition and associated mechanical property enhancement of FeCoCrNi$_{2.1}$Al high entropy alloy, Acta Mater. 252 (2023) 118900, https://doi.org/10.1016/j.actamat.2023.118900.

[29] A.O. Moghaddam, D. Mikhailov, R. Fereidonnejad, N. Shaburova, D. Vinnik, D. Uchaev, D. Uchaev, F.Q. Bai, D. Janas, E. Trofimov, Phase formation, microhardness and magnetic properties of FeNiCrV-TiNb, $(NiCoFeCuMn)_3(AlTi)$ and (FeNiCoCrMn)(MoCr) high entropy intermetallic compounds, J. Alloys Compd. 912 (2022) 165195, https://doi.org/10.1016/j.jallcom.2022.165195.

[30] N. Xu, Y. Yu, W. Zhai, J.Y. Wang, B. Wei, A high-temperature acoustic field measurement and analysis system for determining cavitation intensity in ultrasonically solidified metallic alloys, Ultrason. Sonochem. 94 (2023) 106343, https://doi.org/10.1016/j.ultsonch.2023.106343.

[31] R. Jamshidi, G. Brenner, Dissipation of ultrasonic wave propagation in bubbly liquids considering the effect of compressibility to the first order of acoustical Mach number, Ultrasonics 53 (2013) 842–848, https://doi.org/10.1016/j.ultras.2012.12.004.

[32] J.B. Keller, M. Miksis, Bubble oscillations of large amplitude, J. Acoust. Soc. Am. 68 (1980) 628–633, https://doi.org/10.1121/1.384720.

[33] G. Lebon, G. Salloum-Abou-Jaoude, D. Eskin, I. Tzanakis, K. Pericleous, P. Jarry, Numerical modelling of acoustic streaming during the ultrasonic melt treatment of direct-chill (DC) casting, Ultrason. Sonochem. 54 (2019) 171–182, https://doi.org/10.1016/j.ultsonch.2019.02.002.

[34] W.F. Gale, T.C. Totemeier, Smithells Metals, Elsevier, Amsterdam, 2003.

[35] E.A. Brandes, G.B. Brook, Smithells Metals Reference Book, Butterworth Heinemann, London, 1983.

[36] I. Tzanakis, W.W. Xu, D.G. Eskin, P.D. Lee, N. Kotsovinos, In situ observation and analysis of ultrasonic capillary effect in molten aluminium, Ultrason. Sonochem. 27 (2015) 72–80, https://doi.org/10.1016/j.ultsonch.2015.04.029.

[37] K.A. Jackson, J.D. Hunt, Lamellar and rod eutectic growth, Soc. AIME. 236 (1988) 363–376, https://doi.org/10.1016/B978-0-08-092523-3.50040-X.

[38] W. Kurz, D.J. Fisher, Fundamentals of Solidification, third ed., Trans Tech Publications Ltd., Switzerland, 1992, pp. 22–33.

[39] V.I. Kondaurov, The Clausius-Clapeyron equations for phase transitions of the first kind in a thermoelastic material, J. Appl. Math. Mech. 68 (1) (2004) 65–79, https://doi.org/10.1016/S0021-8928(04)90006-8.

[40] D. Turnbull, R.E. Cech, Microscopic observation of the solidification of small metal droplets, J. Appl. Phys. 21 (8) (1950) 804–810, https://doi.org/10.1063/1.1699763.

[41] C. Cayron, Angular distortive matrices of phase transitions in the fcc-bcc-hcp system, Acta Mater. 111 (2016) 417–441, https://doi.org/10.1016/j.actamat.2016.01.075.

[42] M.P. Kashchenko, V.G. Chashchina, Mechanism of the FCC-BCC martensitic transformation with the fastest rearrangement of close-packed planes. II. Orientation relationships, Russ. Phys. J. 51 (2008) 1161–1167, https://doi.org/10.1007/s11182-009-9150-6.

[43] G. Teufer, The crystal structure of tetragonal ZrO_2, Acta Crystallogr. 15 (1962) 1187, https://doi.org/10.1107/S0365110X62003114, 1187.

[44] S. Morito, H. Tanaka, R. Konishi, T. Furuhara, T. Maki, The morphology and crystallography of lath martensite in Fe-C alloys, Acta Mater. 51 (2003) 1789–1799, https://doi.org/10.1016/S1359-6454(02)00577-3.

[45] L. Jiang, Z.Q. Cao, J.C. Jie, J.J. Zhang, Y.P. Lu, T.M. Wang, T.J. Li, Effect of Mo and Ni elements on microstructure evolution and mechanical properties of the $CoFeNi_xVMo_y$ high entropy alloys, J. Alloys Compd. 649 (2015) 585–590, https://doi.org/10.1016/j.jallcom.2015.07.185.

[46] W.N. Jiao, H. Jiang, D.X. Qiao, J.Y. He, H.L. Zhao, Y.P. Lu, T.J. Li, Effects of Mo on microstructure and mechanical properties of $Fe_2Ni_2CrMo_x$ eutectic high entropy alloys, Mater. Chem. Phys. 260 (2021) 124175, https://doi.org/10.1016/j.matchemphys.2020.124175.

[47] J. Miao, T. Guo, J. Ren, A. Zhang, B. Su, J. Meng, Optimization of mechanical and tribological properties of FCC CrCoNi multi-principal element alloy with Mo addition, Vacuum 149 (2018) 324–330, https://doi.org/10.1016/j.vacuum.2018.01.012.

[48] G. Qin, R.R. Chen, H.T. Zheng, H.Z. Fang, L. Wang, Y.Q. Su, J.J. Guo, H.Z. Fu, Strengthening FCC-CoCrFeMnNi high entropy alloys by Mo addition, J. Mater. Sci. Technol. 35 (2019) 578–583, https://doi.org/10.1016/j.jmst.2018.10.009.

[49] Y. Dong, L. Jiang, Z. Tang, Y. Lu, T. Li, Effect of electromagnetic field on microstructure and properties of bulk $AlCrFeNiMo_{0.2}$ high-entropy alloy, J. Mater. Eng. Perform. 24 (2015) 4475–4481, https://doi.org/10.1007/s11665-015-1727-3.

[50] C.C. Juan, M.H. Tsai, C.W. Tsai, C.M. Lin, W.R. Wang, C.C. Yang, S.K. Chen, S.J. Lin, J.W. Yeh, Enhanced mechanical properties of HfMoTaTiZr and HfMoNbTaTiZr refractory high-entropy alloys, Intermetallics 62 (2015) 76–83, https://doi.org/10.1016/j.intermet.2015.03.013.

[51] Y.X. Zhuang, X.L. Zhang, X.Y. Gu, Effect of annealing on microstructure and mechanical properties of Al0.5CoCrFeMoxNi high-entropy alloys, Entropy 20 (2018) 812, https://doi.org/10.3390/e20110812.

[52] O.N. Senkov, G.B. Wilks, J.M. Scott, D.B. Miracle, Mechanical properties of $Nb_{25}Mo_{25}Ta_{25}W_{25}$ and $V_{20}Nb_{20}Mo_{20}Ta_{20}W_{20}$ refractory high entropy alloys, Intermetallics 19 (2011) 698–706, https://doi.org/10.1016/j.intermet.2011.01.004.

[53] C. Du, F. Maresca, M.G.D. Geers, J.P. Hoefnagels, Ferrite slip system activation investigated by uniaxial micro-tensile tests and simulations, Acta Mater. 146 (2018) 314–327, https://doi.org/10.1016/j.actamat.2017.12.054.

[54] M. Sarebanzadeh, A. Orozco-Caballero, J. Llorca, Accurate determination of active slip systems for improved geometrical criteria of basal-to-basal slip transfer at grain boundaries in pure Mg, Acta Mater. 243 (2023) 118536, https://doi.org/10.1016/j.actamat.2022.118536.

[55] J. Ren, Y. Zhang, D.X. Zhao, Y. Chen, S. Guan, Y.Y. Liu, L. Liu, S.Y. Peng, F.Y. Kong, J.D. Poplawsky, G.H. Gao, T. Voisin, K. An, Y.M. Wang, K.Y. Xie, T. Zhu, W. Chen, Strong yet ductile nanolamellar high-entropy alloys by additive manufacturing, Nature 608 (2022) 62–68, https://doi.org/10.1038/s41586-022-04914-8.